8. C.-J. Yu, G. Richter, A. Datta, M. K. Durbin, P. Dutta, *Phys. Rev. Lett.* **82**, 2326 (1999).
9. J. M. Howe, *Philos. Mag. A* **74**, 761 (1996).
10. S. E. Donnelly, *Radiat. Effects* **90,** 47 (1985).
11. C. Templier, R. J. Gaboriaud, H. Garem, *Mater. Sci. Eng.* **69,** 63 (1984).
12. A. Vom Felde *et al.*, *Phys. Rev. Lett.* **53**, 922 (1984).
13. S. E. Donnelly, C. J. Rossouw, *Science* **230**, 1272 (1985).
14. K. Furuya, N. Ishikawa, C. W. Allen, *J. Microsc.* **194**, 152 (1999).
15. MacTempas; Total Resolution, Berkeley, CA.
16. Experimental and simulated through-focus sequences are available on *Science* Online at www.sciencemag.org/cgi/content/full/1068521/DC1.
17. S. E. Donnelly, K. Furuya, M. Song, R. C. Birtcher, C. W. Allen, *Proceedings of the International Centennial Symposium on the Electron*, A. Kirkland, P. D. Brown, Eds. (Institute of Materials, London, 1999), pp. 306–312.
18. R. C. Birtcher *et al.*, *Phys. Rev. Lett.* **83**, 1617 (1999).
19. S. E. Donnelly *et al.*, unpublished data.
20. The starting point for the fluid Xe simulations was a tetragonal slab of solid, fcc Xe with a lattice parameter 1.5 times that of Al confined between two walls, 8.06 nm apart, each consisting, in the first instance, of three {111} Al planes. The dimensions of the cell were 8.06 nm, 6.86 nm, and 7.43 nm in the [1,1,1], [1,−1,0], and [1,1,−2] directions, respectively, and the crystallographic axes of the Xe were aligned with those of the Al. Periodic boundary conditions were used in the two latter directions. A total of 6720 Xe atoms were used in the simulations. To achieve fluid Xe, the volume of the cell was expanded by 30%, and the temperature was increased to 2000 K for 1 ps, resulting in complete disordering of the Xe layer. The system was then cooled back to 300 K and the simulation continued for a further 10 ps. Two separate simulations were performed: in the first, which was performed with the MOLDY code (*24*), a Lennard-Jones interaction potential was used for all interactions, including the Xe-Al interaction. With this approach, however, equipotential surfaces near the interface were corrugated due to the individual atoms in the interface. This gave rise to a keying effect that resulted in ordering in the first Xe layer that was visible in the simulated images; however, such ordering was not observed in the experimental images. The second approach was to replace the three Al layers by a planar repulsive potential of the form $V(R) = c/R^{12}$, where R is the distance from the facet and c was chosen to give equivalence to the repulsive term in the Lennard-Jones potential. This simulation was performed with the DLPOLY code (*25*) with an adaptation of the external field routine to represent the planar confining potential. This gave rise to equipotential surfaces that were flat. A realistic Xe-Al potential, which is not currently available, would result in equipotential surfaces between these two extremes. The planar potential was also used for all six facets in the simulation of the small cubic cavity. Although both simulations are physically unrealistic as far as the Xe-Al interaction is concerned, in addition to inducing ordering in the first Xe layer, the effect of changing the Al-Xe potential is to change the separation between the Xe and Al interface layers. Hence in this work, the separation between the first Xe layer and the Al layers has no quantitative importance.
21. M. Schmidt, H. Löwen, *Phys. Rev. E* **55**, 7228 (1997).
22. W. K. Kegel, H. Reiss, H. N. W. Lekkerkerker, *Phys. Rev. Lett.* **83**, 5298 (1999).
23. Although metastable Cu precipitates with a bcc structure have been identified in irradiated Fe alloys, it is likely that factors other than the confining geometry may play a role in this system (*26*).
24. K. Refson, *Comput. Phys. Commun.* **126**, 310 (2000).
25. W. Smith, T. R. Forester, *J. Mol. Graphics* **14**, 136 (1996).
26. S. Pizzini, K. J. Roberts, W. J. Pythian, C. A. English, G. N. Greaves, *Philos. Mag. Lett.* **61**, 223 (1990).
27. Density is determined from the number of atoms contained in a tetragonal box whose faces are located half way between the surface layers and the second layer in each direction. This avoids problems associated with defining the volume associated with the surface atoms.
28. S.E.D., R.C.B., C.W.A., and U.D. acknowledge funding from the National Institute for Materials Science, for collaborative visits to Japan; S.E.D. acknowledges funding from the Materials Science Division at Argonne National Laboratory for extended visits to the laboratory.

29 November 2001; accepted 12 March 2002
Published online 21 March 2002;
10.1126/science.1068521
Include this information when citing this paper.

External Reflection from Omnidirectional Dielectric Mirror Fibers

Shandon D. Hart,[1] Garry R. Maskaly,[1] Burak Temelkuran,[1,3] Peter H. Prideaux,[3] John D. Joannopoulos,[2,3] Yoel Fink[1,3]*

We report the design and fabrication of a multilayered macroscopic fiber preform and the subsequent drawing and optical characterization of extended lengths of omnidirectional dielectric mirror fibers with submicrometer layer thickness. A pair of glassy materials with substantially different indices of refraction, but with similar thermomechanical properties, was used to construct 21 layers of alternating refractive index surrounding a tough polymer core. Large directional photonic band gaps and high reflection efficiencies comparable to those of the best metallic reflectors were obtained. Potential applications of these fibers include woven fabrics for radiation barriers, spectral authentication of cloth, and filters for telecommunications.

Polymer fibers are ubiquitous in applications such as textile fabrics because of their excellent mechanical properties and the availability of low-cost, high-volume processing techniques; however, control over their optical properties has so far remained relatively limited. Conversely, dielectric mirrors are used to precisely control and manipulate light in high-performance optical applications, but the fabrication of these typically fragile mirrors has been mostly restricted to planar geometries and remains costly. We combined some of the advantages of each of these seemingly dissimilar products in the fabrication of polymeric fibers with an exterior multilayer dielectric mirror. Thermal processing techniques were used to reduce a macroscopic layered dielectric structure to submicrometer length scales, creating a fiber having a photonic band gap in the mid-infrared (mid-IR). Where previous experimental and theoretical work on multilayer fibers has focused on the purpose of light transmission through a hollow core (*1–3*), we used multiple dielectric layers on the exterior of a mirror fiber to create the potential for new conformal reflector functionality (*4*). These fibers could be incorporated into woven fabrics for precise spectral identity verification, such as a unique optical bar code; they could also be used as flexible radiation barriers or as filters in telecommunications.

A typical dielectric mirror (also called a one-dimensional photonic crystal) is a planar stack of dielectric layers made of two alternating materials with different refractive indices. Although these mirrors do not possess a complete photonic band gap, it has been shown that they can be designed to efficiently reflect light of all incident angles and polarizations across broad, selectable frequency ranges (*5, 6*). This advance has inspired interest in the use of omnidirectional dielectric mirrors in applications requiring optimal confinement or reflection of light at all external angles, such as optical cavities or hollow waveguides. The theory and properties of planar multilayer dielectric mirrors and omnidirectional reflectors have been explored elsewhere (*5–10*).

The degree of use of all types of dielectric mirrors has been impeded by the cost and complexity associated with their fabrication and by the difficulties associated with depositing these mirrors on nonplanar surfaces. Weber and coworkers (*11*) reported the fabrication of free-standing, graded-thickness polymeric dielectric mirrors with relatively low-refractive-index contrast between adjacent birefringent layers. The system employed in our work uses amorphous materials having high-refractive-index contrast. This has some advantages over a low-contrast structure in that the evanescent decay lengths and electric field power densities of reflected electromagnetic (EM) waves are much smaller in the mirror stack, making it

[1]Department of Materials Science and Engineering, [2]Department of Physics, [3]Research Laboratory of Electronics, Massachusetts Institute of Technology, Cambridge, MA 02139, USA.

*To whom correspondence should be addressed.

possible to achieve high reflectivity with relatively few layers. The reduced material-light interaction brought about by this high-refractive-index contrast also reduces material absorption. One strategy commonly used to achieve high-index contrast has been to fabricate porous photonic crystal structures with air as the low-index component (*12*). Although this approach yields large-index contrast, there remain some limitations associated with the formation of large interfacial areas prone to contamination and interconnected structures that may be mechanically weak. The materials system we describe here could be used to create high-index-contrast photonic crystal structures having periodicity along one, two, or three axes (*13*); these structures may be mechanically tough and need not maintain high physical connectivity within either the high- or low-index component.

We employed a three-pronged approach in omnidirectional dielectric mirror fiber production, consisting of materials identification, fiber preform construction, and fiber draw. Materials selection involved the empirical identification of a pair of amorphous materials, poly(ether sulfone) (PES) and arsenic triselenide (As_2Se_3), which have substantially different refractive indices, yet similar thermomechanical properties within a certain thermal processing window. Amorphous or glassy materials lack the abrupt change in viscosity with temperature associated with crystalline materials at their melting point, because of the absence of a first-order thermodynamic transition when a melt is cooled to the glassy state. This continuous viscosity variation is one of the most important factors that allow inorganic glasses and organic thermoplastics to be formed by high-speed thermal processes such as drawing, blowing, pressing, and extrusion (*14, 15*). In order to use similar processes in the fabrication of omnidirectional mirror structures, the selected materials should exhibit low optical absorption over a common wavelength band, very similar viscosities at the processing temperatures of interest, and good adhesion/wetting without cracking, even when subjected to thermal quenching.

Adhesion and extensional viscosity under melt conditions are difficult to measure in general, and the measurement of high-temperature surface tension is quite involved (*16*). Thus, limited data on these properties are available, and it was necessary to empirically identify materials that could be used to draw our mirror fibers. Various high-index chalcogenide (S-, Se-, and Te-containing) glasses and low-index polymers were identified as potential candidates on the basis of their optical properties and overlapping thermal softening regimes. Adhesion and viscosity matching were tested by thermal evaporation of a chalcogenide glass layer on top of a polymer film or rod and elongation of the coated substrate at elevated temperatures. The choice of a high-temperature polymer, PES, and a simple chalcogenide glass, As_2Se_3, resulted in excellent thermal codeformation without film cracking or delamination. Approximate matching of extensional viscosity in this manner was also demonstrated with As_2Se_3 and poly(ether imide). The properties, processing, and applications of chalcogenide glasses have been explored extensively elsewhere (*17–21*). One advantage in choosing As_2Se_3 for this application is that not only is it a stable glass, but it is a stoichiometric compound that can be readily deposited in thin films through thermal evaporation or sputtering without dissociation (*17*). Additionally, As_2Se_3 is transparent to IR radiation from approximately 0.8 to 17 μm and has a refractive index of ~2.8 in the mid-IR (*22*). PES is a high-performance, dimensionally stable thermoplastic with a refractive index of ~1.55 and good transparency to EM waves in a range extending from the visible regime into the mid-IR (*23, 24*).

The selected materials were used to construct a multilayer preform rod, which essentially is a macroscale version of the final fiber. To fabricate the dielectric mirror fiber preform, we deposited an As_2Se_3 film through thermal evaporation on either side of a free-standing PES film, which was then rolled on top of a PES tube substrate, forming a structure with 21 alternating layers of PES and As_2Se_3, using only four vapor deposition steps (*25*). The resulting multilayer fiber preform was subsequently thermomechanically drawn down with an optical fiber draw tower (*14, 26*) into hundreds of meters of multilayer fiber with precisely controlled submicrometer layer thickness, creating a photonic band gap in the mid-IR. Fibers of outer diameters (ODs) varying from 175 to 500 μm with a typical standard deviation of 10 μm from target were drawn from the same preform to demonstrate adjustment of the reflectivity spectra through thermal deformation. The spectral position of the photonic band gap was controlled by the optical monitoring of the OD of the fiber during draw, which was later verified by reflectivity measurements on single and multiple fibers of different diameters.

In theoretically predicting the spectral response of these fibers, it is helpful to calculate the photonic band structure that corresponds to an infinite one-dimensional photonic crystal (Fig. 1); this allows for the analysis of propagating and evanescent modes in the structure, corresponding to real or imaginary Bloch wave number solutions (*5–7*). The electric or magnetic field vector is parallel to the mirror layer interfaces for the transverse electric and transverse magnetic polarized modes, respectively. The parallel wave vector k_y is the component of the incident EM wave vector that is parallel to the layer interfaces. The phase space accessible from an external ambient medium is contained between the light lines (defined by the glancing-angle condition $\omega = ck_y/n_0$, where c is the speed of light in a vacuum, and n_0 is the refractive index of the ambient medium), and the modes between the 35° lines correspond

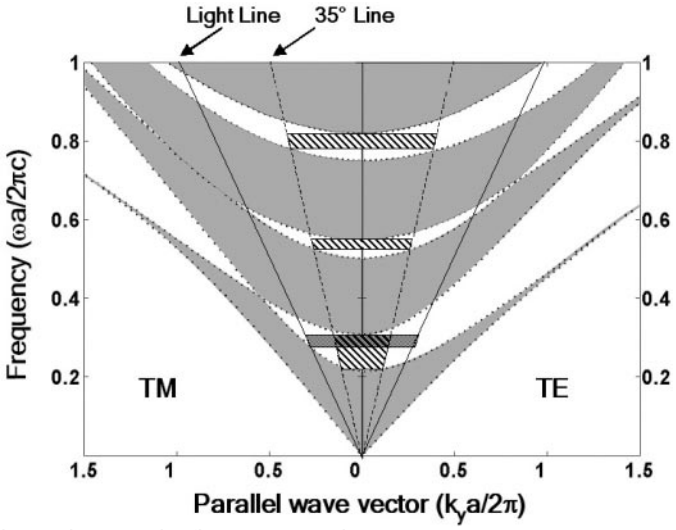

Fig. 1. Photonic band diagram for a one-dimensional photonic crystal having a periodic refractive index alternating between 2.8 and 1.55. Gray regions represent propagating modes within the structure, and white regions represent evanescent modes. Hatched regions represent photonic band gaps where high reflectivity can be expected for external EM waves over an angular range extending from normal to 35° incidence. The shaded trapezoid represents a region of external omnidirectional reflection. TM and TE represent transverse magnetic and transverse electric polarized modes, respectively.

Table 1. Calculated and experimental photonic band gap positions for fibers drawn to a 400-μm OD. Calculated values were obtained with the normalized frequency values of the photonic band diagram (Fig. 1), together with the bilayer thickness of a = 0.90 μm measured through SEM imaging. Experimental values were obtained from spectral measurements (Fig. 3A).

Photonic band gap	Calculated central wavelength (μm)	Experimental central wavelength (μm)
First	3.35	3.4
Second	1.7	1.65
Third	1.1	1.1

to those sampled experimentally. Axes are normalized to the thickness a of one mirror bilayer (a period consisting of one high-index and one low-index layer). The photonic band diagram for an infinite structure having periodicity and refractive indices similar to those of the fabricated mirror structures is shown in Fig. 1. Three photonic band gaps are present where high reflectivity is expected within the 0 to 35° angular range, and the fundamental gap contains a region of external omnidirectional reflectivity.

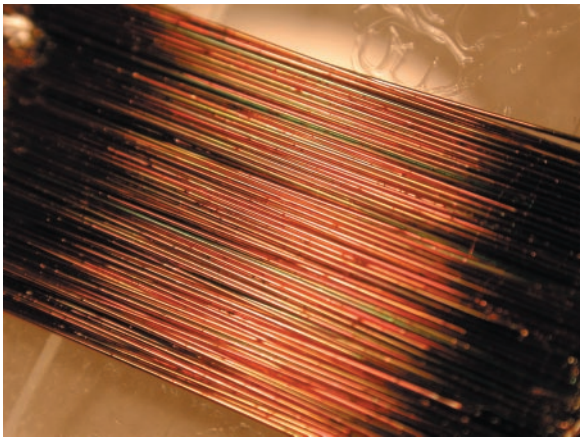

Fig. 2. Parallel fiber array made from 200-μm-OD fibers used to obtain reflectivity data presented in Fig. 3B. Sections of ~5-cm length were cut from a single continuous fiber to make the array. Although As_2Se_3 is highly absorbing in the visible regime, some iridescent colors are visible to the naked eye.

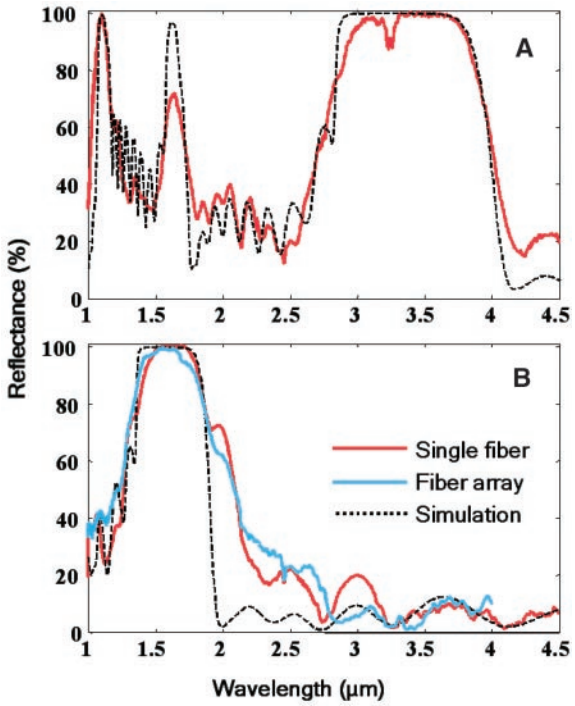

Fig. 3. Measured reflectance spectra for (**A**) 400-μm-OD and (**B**) 200-μm-OD dielectric mirror fibers relative to gold-coated fibers of the same diameter. A single-fiber reflectivity measurement is shown in (A), whereas (B) compares single-fiber reflectivity to that measured from a multifiber array. Simulations were performed with the transfer matrix method.

Mirror fiber reflectivity was measured from both single fibers and parallel fiber arrays (Fig. 2) with a Nicolet/SpectraTech NicPlan infrared microscope and Fourier transform infrared spectrometer (Magna 860). The microscope objective (SpectraTech ×15, Reflachromat) used to focus on the fibers had a numerical aperture (NA) of 0.58. This resulted in a detected cone where the angle of reflection with respect to the surface normal of the structure could vary from normal incidence to ~35°, which is determined by the NA of the microscope objective (*27*). As a background reference for the reflection measurements, we used gold-coated PES fibers of matching diameters. Dielectric mirror fibers drawn to a 400-μm OD exhibited a very strong reflection band centered at a wavelength of 3.4 μm (Fig. 3A). Measured reflectivity spectra agree well with planar-mirror transfer matrix method simulations [see, for example, (*28*)], where the reflectivity was averaged across the aforementioned angular range for both polarization modes. Fibers drawn down to a 200-μm OD show a similar strong fundamental reflection band centered near 1.7 μm (Fig. 3B). This shifting of the primary photonic band gap illustrates the precise tuning of the reflectivity spectra over wide frequency ranges through thermal deformation processing. Strong optical signatures are measurable from single fibers as small as 200 μm in OD. Fiber array measurements, simultaneously sampling reflected light from multiple fibers, agree well with single-fiber data (Fig. 3B).

These reflectivity results are strongly indicative of uniform layer thickness control, good interlayer adhesion, and low interdiffusion through multiple thermal treatments. This was confirmed by scanning electron microscope (SEM) inspection of fiber cross sec-

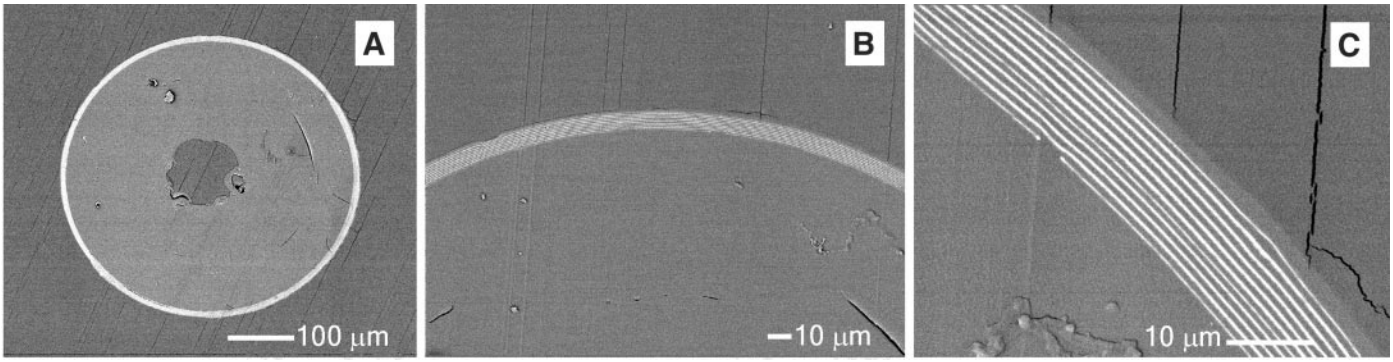

Fig. 4. (**A** to **C**) SEM micrographs of a 400-μm-OD fiber cross section embedded in epoxy. The entire fiber cross section is shown in (A), with mirror structure surrounding the PES core; (B) demonstrates that most of the fiber exterior is free of substantial defects and that the mirror structure adheres well to the fiber substrate; and (C) reveals the ordering and adhesion within the alternating layers of As_2Se_3 (bright layers) and PES. Stresses developed during sectioning caused some cracks in the mounting epoxy that are deflected at the fiber interface. Fibers from this batch were used in the reflectivity measurements recorded in Fig. 3A.

tions (Fig. 4). The layer thicknesses observed (a = 0.90 μm for the 400-μm fibers; a = 0.45 μm for the 200-μm fibers) correspond well to the measured reflectivity spectra. The fibers have a hole in the center, because of the choice of a hollow rod as the preform substrate, which experienced some nonuniform deformation during draw. The rolled-up mirror structure included a double outer layer of PES for mechanical protection, creating a noticeable absorption peak in the reflectivity spectrum at ~3.2 μm (Fig. 3A).

A combination of spectral and direct imaging data demonstrates excellent agreement with the photonic band diagram. Table 1 summarizes this agreement for the 400-μm-OD fibers by comparing the calculated photonic band gap locations shown in Fig. 1, together with the SEM-measured period spacing of a = 0.90 μm, to the empirical spectral reflection data shown in Fig. 3A. The measured gap width (range to midrange ratio) of the fundamental gap for the 400-μm-OD fiber is 27%, compared to 29% in the photonic band diagram.

In light of these results, we can evaluate the relative importance of various physical properties in creating these drawn omnidirectional dielectric mirror fibers. The matching of rheological behavior in elongation at the draw temperature is the key factor in our fiber production. At the draw temperature, the materials should be fluid enough to elongate without sizable stress buildup, yet not so fluid that the mirror layers lose their periodicity. Coefficient of thermal expansion (CTE) may also play an important role in the adhesion and integrity of thin films during any thermal quenching procedure. PES has a linear CTE of 55 × 10^{-6}/°C (*23*), whereas As_2Se_3 has a linear CTE of 25 ×10^{-6}/°C (*22*). In the mirror fiber geometry described here, this CTE mismatch could act to strengthen the outer As_2Se_3 layers by placing them in compression as the PES core of the fiber cools and contracts well below the glass transition of As_2Se_3. This materials combination facilitated the thermal fabrication of high-performance dielectric mirrors in a conformal, flexible fiber geometry.

References and Notes

1. P. Yeh, A. Yariv, E. Marom, *J. Opt. Soc. Am.* **68**, 1196 (1978).
2. J. W. Dai, J. A. Harrington, *Appl. Opt.* **36**, 5072 (1997).
3. Y. Fink *et al.*, *J. Lightwave Technol.* **17**, 2039 (1999).
4. We are also pursuing the application of the types of materials and methods described here to the fabrication of hollow fibers having multiple dielectric layers surrounding a hollow core for the purpose of light guidance.
5. Y. Fink *et al.*, *Science* **282**, 1679 (1998).
6. J. N. Winn, Y. Fink, S. Fan, J. D. Joannopoulos, *Opt. Lett.* **23**, 1573 (1998).
7. P. Yeh, A. Yariv, C. Hong, *J. Opt. Soc. Am.* **67**, 423 (1977).
8. B. Temelkuran, E. L. Thomas, J. D. Joannopoulos, Y. Fink, *Opt. Lett.* **26**, 1370 (2001).
9. H. F. Mahlein, *J. Opt. Soc. Am.* **64**, 647 (1974).
10. P. Baumeister, *Opt. Acta* **8**, 105 (1961).
11. M. F. Weber, C. A. Stover, L. R. Gilbert, T. J. Nevitt, A. J. Ouderkirk, *Science* **287**, 2451 (2000).
12. R. F. Cregan *et al.*, *Science* **285**, 1537 (1999).
13. J. D. Joannopoulos, R. Meade, J. N. Winn, *Photonic Crystals: Molding the Flow of Light* (Princeton Univ. Press, Princeton, NJ, 1995).
14. A. K. Varshneya, *Fundamentals of Inorganic Glasses* (Academic Press, San Diego, CA, 1994).
15. D. W. Van Krevelen, *Properties of Polymers* (Elsevier Scientific, New York, ed. 3, 1990).
16. A. Kucuk, A. G. Clare, L. Jones, *Glass Technol.* **40**, 149 (1999).
17. Z. U. Borisova, *Glassy Semiconductors* (Plenum, New York, 1981).
18. A. K. Varshneya, *J. Non-Cryst. Solids* **273**, 1 (2000).
19. A. B. Seddon, *J. Non-Cryst. Solids* **184**, 44 (1995).
20. W. A. King, A. G. Clare, W. C. LaCourse, *J. Non-Cryst. Solids* **181**, 231 (1995).
21. A. R. Hilton, *J. Non-Cryst. Solids* **2**, 28 (1970).
22. M. Bass, Ed., *Handbook of Optics* (McGraw-Hill, New York, 1995).
23. J. E. Mark, Ed., *Polymer Data Handbook* (Oxford Univ. Press, New York, 1999).
24. C. Sarantos, unpublished data.
25. PES films were purchased from the Goodfellow Corporation, and As_2Se_3 (99.999% pure, metals basis) was purchased from Alfa Aesar/Strem Chemicals. A 2-cm-OD PES rod was made from a PES film of 50 ± 5 μm that was rolled by hand onto a 7-mm hollow borosilicate glass tube and consolidated through heat treatment at 261° to 263°C under vacuum for ~25 min. As_2Se_3 films were deposited by thermal evaporation with a vacuum evaporator (Ladd Industries) on a separate PES film. In situ layer thickness monitoring was carried out with a crystal thickness monitor (Sycon STM100) that was calibrated with a surface profilometer (Tencor P10). An As_2Se_3 film of 6.5 ± 0.4 μm was evaporated at a rate of ~10 nm/s on each side of a thin PES film of 25 ± 2 μm. This As_2Se_3-coated film was then rolled onto the outside of the previously fabricated PES tube and consolidated with a similar vacuum thermal treatment. The hollow Pyrex tube at the core of the PES/As_2Se_3 structure was then etched out with hydrofluoric acid.
26. The preform was lowered at a controlled rate into a three-zone vertical tube furnace (Thermcraft) and pulled from below at controlled speeds with a motorized capstan (Heathway). Fiber diameters were monitored with laser diameter monitors (Beta LaserMike). Fibers were drawn at a central-zone maximum temperature of 295°C at speeds ranging from approximately 1 to 10 m/min, depending on target fiber diameter. The upper zone of the furnace was heated to 240°C, and the lower zone was unheated, but drifted to a temperature of ~150°C.
27. The applicability of the indicated angular range of detection was corroborated by personal communication with M. Friedman of SpectraTech.
28. J. A. Kong, *Electromagnetic Wave Theory* (EMW Publishing, Cambridge, MA, 2000), pp. 370–406.

29. We thank H. Burch for guidance and inspiration; C. H. Sarantos, K. R. Maskaly, E. P. Chan, and M. Frongillo for valuable assistance; and J. Harrington, A. R. Hilton, and E. L. Thomas for support and direction. We also thank K. Hersey, B. Smith, and the MIT Research Laboratory of Electronics for their support. G.R.M. thanks the Fannie and John Hertz Foundation for its support. This work was supported under the following awards: Army Research Office/Defense Advanced Research Projects Agency award DAAD19-01-1-0647; NSF award ECS 0123460; and U.S. Department of Energy award DE-FG02-99ER45778. This work was also supported in part by the Materials Research Science and Engineering Center (MRSEC) program of NSF award DMR 98-08941 and made use of MRSEC shared facilities supported by NSF under award DMR-9400334. This material is also based on work supported in part under an NSF graduate research fellowship. Special thanks are also given to U. Kolodny and OmniGuide Communications, Inc.

22 January 2002; accepted 13 March 2002

Superplumes from the Core-Mantle Boundary to the Lithosphere: Implications for Heat Flux

Barbara Romanowicz,* Yuancheng Gung

Three-dimensional modeling of upper-mantle anelastic structure reveals that thermal upwellings associated with the two superplumes, imaged by seismic elastic tomography at the base of the mantle, persist through the upper-mantle transition zone and are deflected horizontally beneath the lithosphere. This explains the unique transverse shear wave isotropy in the central Pacific. We infer that the two superplumes may play a major and stable role in supplying heat and horizontal flow to the low-viscosity asthenospheric channel, lubricating plate motions and feeding hot spots. We suggest that more heat may be carried through the core-mantle boundary than is accounted for by hot spot fluxes alone.

Global seismic tomography aims to improve our understanding of mantle dynamics by providing constraints on three-dimensional (3D) temperature and composition with the use of elastic velocities as proxies. Much progress has been made in recent years in resolving increasingly finer details in the 3D distribution of elastic velocities from the inversion of seismic phase and travel time data (*1–3*). In particular, regions of faster-than-average velocity, associated with subduction around the Pacific rim, have revealed a variety of behaviors of lithospheric slabs in the transition zone, some stag-

Seismological Laboratory, University of California, Berkeley, 215 McCone Hall, Berkeley, CA 94720, USA.

*To whom correspondence should be addressed. E-mail: barbara@seismo.berkeley.edu